THE UNIVERSITY of EDINBURGH

Edinburgh Research Explorer

A novel diamond anvil cell for X-ray diffraction at cryogenic temperatures manufactured by 3D printing

OPEN ACCESS

A novel diamond anvil cell for x-ray diffraction at cryogenic temperatures manufactured by 3D printing

H. Jin,[1] C. H. Woodall,[1] X. Wang,[1] S. Parsons,[2] and K. V. Kamenev[1,a)]

[1]*School of Engineering and Centre for Science at Extreme Conditions, The University of Edinburgh, Edinburgh EH9 3FD, United Kingdom*
[2]*School of Chemistry and Centre for Science at Extreme Conditions, The University of Edinburgh, Edinburgh EH9 3FJ, United Kingdom*

A new miniature high-pressure diamond anvil cell was designed and constructed using 3D micro laser sintering technology. This is the first application of the use of rapid prototyping technology to construct high-pressure apparatus. The cell is specifically designed for use as an X-ray diffraction cell that can be used with commercially available diffractometers and open-flow cryogenic equipment to collect data at low temperature and high pressure. The cell is constructed from stainless steel 316L and is about 9 mm in diameter and 7 mm in height, giving it both small dimensions and low thermal mass, and it will fit into the cooling envelope of a standard Cryostream^{TM} cooling system. The cell is clamped using a customized miniature buttress thread of diameter 7 mm and pitch of 0.5 mm enabled by 3D micro laser sintering technology; such dimensions are not attainable using conventional machining. The buttress thread was used as it has favourable uniaxial load properties allowing for higher pressure and better anvil alignment. The clamp can support the load of at least 1.5 kN according to finite element analysis (FEA) simulations. FEA simulations were also used to compare the performance of the standard thread and the buttress thread, and demonstrate that stress is distributed more uniformly in the latter. Rapid prototyping of the pressure cell by the laser sintering resulted in a substantially higher tensile yield strength of the 316L stainless steel (675 MPa compared to 220 MPa for the wrought type of the same material), which increased the upper pressure limit of the cell. The cell is capable of reaching pressures of up to 15 GPa with 600 μm diameter culets of diamond anvils. Sample temperature and pressure changes on cooling were assessed using X-ray diffraction on samples of NaCl and HMT-d$_{12}$. © *2017 Author(s). All article content, except where otherwise noted, is licensed under a Creative Commons Attribution (CC BY) license (http://creativecommons.org/licenses/by/4.0/).* [http://dx.doi.org/10.1063/1.4977486]

I. INTRODUCTION

Most high-pressure research is conducted using diamond anvil cells (DACs) in which two opposing anvils are brought together to deform a gasket material, thus generating a quasi-hydrostatic pressure within a sample cavity. X-ray diffraction is a common method for probing the pressurized state within the sample volume up to pressures of the order of 100 GPa.[1] DACs are particularly suited to such measurements due to their relatively small size, which allows them to be mounted on diffractometers, and the large pressures they can generate. Typically, Merrill-Bassett type cells[2] are used for such diffraction measurements, but in recent years other cell designs have become increasingly popular in other areas of high-pressure research, such as the turnbuckle design first developed for use in high-pulsed magnetic fields[3,4] and for magnetic measurements in commercial magnetometers.[5,6] Although some miniature DACs for X-ray work have been constructed for use in cryogenic experiments,[7,8] there is a scope for further miniaturization to enable the use of open-flow cryogenic equipment which is practically extremely convenient and very commonly

available, but which has limited volume or cooling power compared to closed cryostats.

When miniaturizing high-pressure cells, it is important to consider possible construction difficulties. Conventional manufacturing processes are subject to a number of limitations such as complex geometry and the dimensional limits for small features such as very small threads. Furthermore, the residual material from the cutting tools embedded on the surface of the parts can cause undesirable effects such as a high background signal in magnetic measurements or other experiments, which are sensitive to particular material properties.

In recent years, the development of additive manufacturing technologies[9] has provided increased freedom for engineers when designing parts, allowing the construction of complex geometries, previously unattainable via conventional means. Selective laser sintering,[10] in which metal powders are melted and sintered by lasers, layer by layer is one of these technologies. Recent studies have shown that the mechanical properties of some laser sintered metals can exceed those of the wrought metals. For example, 3D printed stainless steel 316L has a higher tensile yield strength and ultimate tensile strength compared to the same material in its wrought form[11] (Table I). The high temperature gradient and quick solidification involved in selective laser sintering create a steel

a)Electronic mail: K.Kamenev@ed.ac.uk

TABLE I. The mechanical properties of MLS 316L and wrought 316L.[12]

Mechanical properties	MLS 316L	Wrought 316L
Tensile yield strength (MPa)	675	220
Ultimate tensile strength (MPa)	746	517
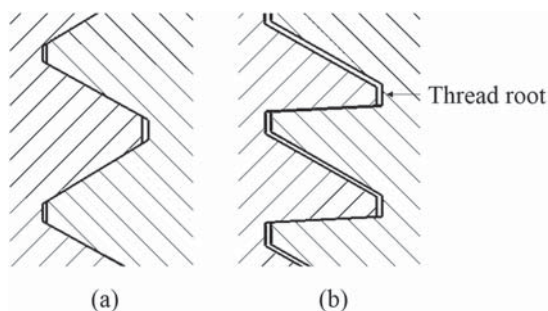
FIG. 1. Schematic drawing of a standard metric ISO profile (a) and a buttress (b) thread.

FIG. 2. The CAD rendered view of the 3D-DAC assembly.

with more refined microstructure compared to conventional manufacturing, resulting in enhanced mechanical properties.

Furthermore, with the development of micro laser sintering (MLS) technology, the dimensional tolerance of components can be as good as ± 5 μm, which is precise enough for most applications, including miniature pressure cells. Small features such as threads can be modified, optimized, and manufactured by the MLS method to improve the load support capability of the cell. As an example, we will consider a buttress thread (Fig. 1(b)), which is used in high-pressure cells for its favorable performance in applications with extremely high unidirectional stress along the thread axis.[13] The radial components of the thrust can be minimized and a better alignment can be achieved because the pressure flank is almost perpendicular to the thread axis. This feature of the buttress thread has been utilized in large volume pressures cells such as the Paris-Edinburgh press to improve the load support capability and the alignment.[14] However, the limitations imposed by conventional manufacturing methods make it difficult to machine buttress threads with small pitches on smaller cells, and the minimum pitch of commercially available buttress thread machining tools is 0.8 mm. In this work, we overcome the limitations imposed by conventional manufacturing techniques and present the first 3D printed high-pressure cell (3D-DAC) for X-ray diffraction at low temperatures.

II. 3D-DAC DESIGN

The 3D-DAC is designed for X-ray diffraction experiments at low temperatures generated by the popular Cryostream gas-flow device from Oxford Cryosystems.[15] Cryostream operates by blowing a stream of cold nitrogen gas onto the sample mounted on a goniometer head. The cross section of the gas stream is 10 mm in diameter and the pressure cell should be small enough to be fully enclosed by the stream of gas in order to provide efficient cooling and avoid surface icing. In addition to overall dimensional constraints, single crystal X-ray diffraction experiments demand a large opening angle on both sides of the cell to ensure collection of data
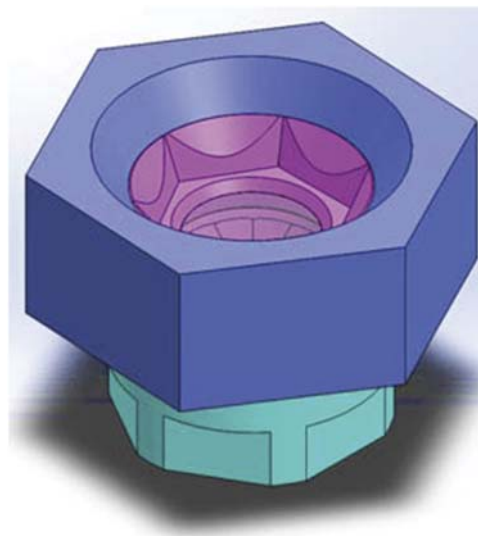
within a large portion of reciprocal space. In order to satisfy these criteria, the cell was designed around the Boehler-Almax diamond anvils[16] with an opening angle of 80°. The material of the cell should have high thermal conductivity to provide efficient cooling of the sample and be corrosion-resistive to avoid rusting due to moisture condensing during thermal cycling.

The overall design of the 3D-DAC is presented in Figs. 2 and 3. The bottom diamond anvil is supported by the body of the cell while the top anvil is mounted in the seat, which is clamped by the nut. The loading procedure and the operational principles are described below. Here we focus on the elements of the cell design.

In order to make the cell as small as possible, only one threaded connection was used in preference to two as in the turnbuckle design. In the turnbuckle cell design,[6] the pitches of both the top and bottom threads are 0.5 mm, and so the equivalent pitch for the overall cell is effectively 1 mm. This means that when the body of the turnbuckle cell turns one full circle, the total vertical displacement of the top and bottom nuts towards each other is 1 mm. The advantage of one threaded connection is that the real pitch for the cell is the same as the
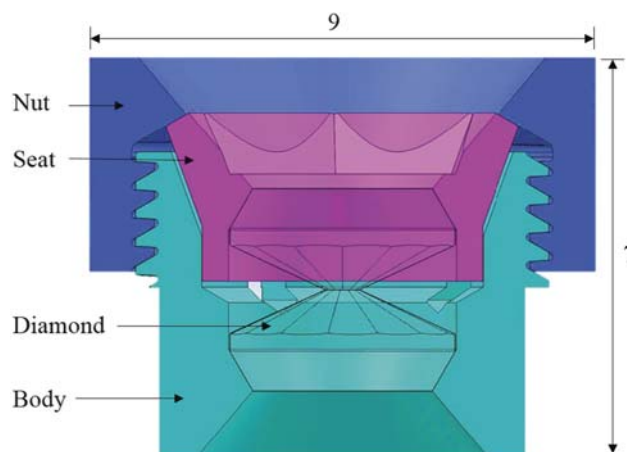

FIG. 3. The cross-sectional view of the CAD model of the cell with key dimensions (in mm).
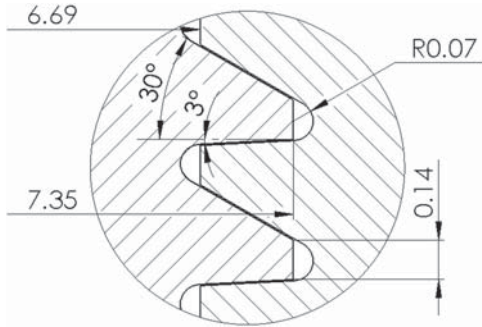
FIG. 4. The parameters of the customized buttress thread used in this design (mm).

FIG. 6. The final printing sequences of the cell components. The red line is the base-line of the printing process, and the red arrow is the direction of the printing process.

pitch of the thread, which is only 0.5 mm. Therefore, an additional advantage of this design is that it allows the pressure to be changed to smaller, more stable and controllable increments than in miniature DACs based on two-threaded connections.[6,7]

The optimal type of the thread for axial load engineering applications is a buttress thread. In the absence of any other alignment mechanisms, the buttress thread aids the alignment of the anvils because the flank supporting the load is nearly perpendicular to the axis of the thread. In addition, compared to the other types of threads, the buttress thread can be used to obtain a greater strength at the root.[17] However, the minimum pitch of commercially available buttress thread machining tools is 0.8 mm, which is a rather coarse pitch in the context of the present application. Use of 3D printing technology enables manufacturing of finer custom designed threads. The thread was initially customized using finite element analysis (FEA) modeling in conjunction with DIN-20401-2004 for buttress threads (Fig. 4).

Although MLS can be used to create complex shapes, it places its own constraints on component geometry, and the

aspect ratio for pins, holes, and wall thicknesses thus need to follow the requirements of the specific 3D printing technologies being used.[18] It is also important to consider carefully the sequence of the printing process. Powders are sintered during the MLS process using support structures, but unsupported areas, such as the back surfaces of overhangs, can suffer
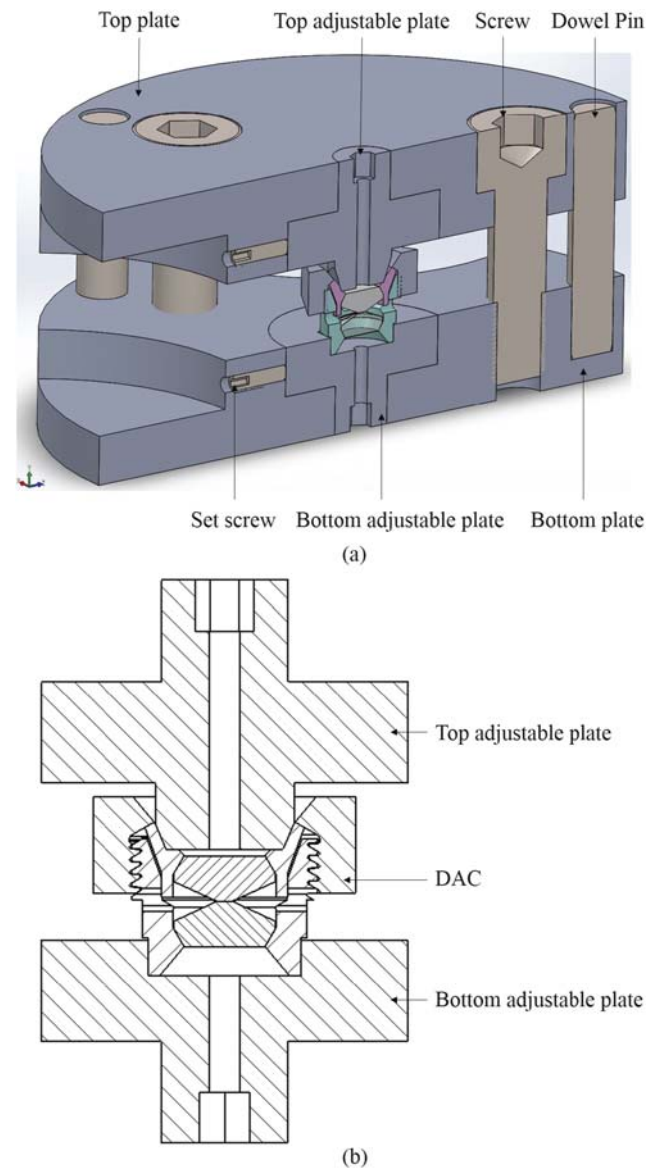
FIG. 7. (a) The rendered view of the assembly of the cell and the clamp. (b) The cross-sectional view of the CAD model of the DAC and two adjustable plates. Three screws are used to apply load on the DAC. The top and bottom adjustable plates, each of which is aligned and clamped by a set of three set screws, are used to restrict the rotation of the cell when the nut is rotated to lock the pressure.
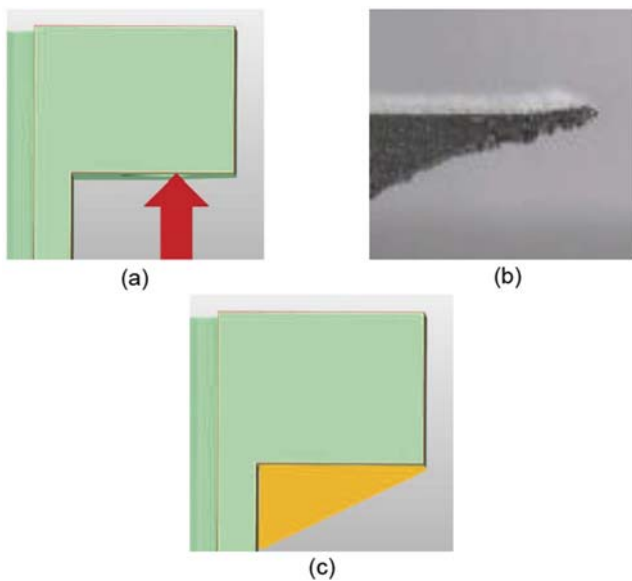

FIG. 5. (a) An example of an overhang structure (green component) in the MLS process. The red arrow shows the direction of the printing process. (b) The sintered back surface of the overhang structure without supports. (c) Overhang structures should be supported by additional structures (yellow component) during the MLS process. The angle of the supports from the horizontal plane should be higher than 30°.[18]

from poor sintering (Fig. 5). This would occur, for example, if printing of two buttress threads was to be attempted in a turnbuckle design: one of the threads would become an overhang because of the symmetrical geometry of the two threads. Printing sequences therefore need to be formulated to avoid these problems. The final printing sequences of the cell components are in Fig. 6.

The assembly of the cell and the clamp is shown in Fig. 7. The pressure cell is placed into a specially designed clamp[19] for increasing pressure and clamping the load (Fig. 7(a)). The clamp has two adjustable plates to fit into the body and the nut of the cell, which constrain the rotation of the cell when the nut is rotated to lock the pressure. Hexagonal geometry is used at both ends of the cell to supply sufficient torsion when the nut is rotated. However, on the top of the cell, the seat part does not have enough thickness for a conventional straight hexagonal cut-out. In order to keep the seat robust enough to withstand the torque during clamping, an angled hex profile was used. A straight hexagon geometry is used on the end of the body part to supply sufficient torque during the loading. The clamp provides optical access through the holes in the top and bottom adjustable plates (Fig. 7(b)) to the sample cavity, enabling the use of ruby fluorescence to measure pressure. The culet size of the diamond was chosen to be 600 μm because this provides a conveniently sized cavity for single crystal diffraction measurement using in-house equipment.

III. FINITE ELEMENT ANALYSIS

The stress distribution in the cell components should be estimated or calculated, prior to the construction of the cell, in order to minimize its dimensions as well as to determine the bearing capability of the cell, optimize the design, and compare the performance between the customized buttress and the standard threads. Due to the complicated geometric shapes of the anvils and the thread, the accurate stress calculations are challenging with analytical equations. Therefore, FEA modelling is used in this project.

A. FEA model

Of the various components of the cell, the thread has the lowest wall thickness and in addition the stress is concentrated at the roots. The likely failure points can thus be expected to appear at the thread. In addition, since the stress distribution is not fully axisymmetric, especially at the undercut of the thread, a 3D FEA model was built to conduct the simulation. In order to reduce the computational time, only the body part and the nut part were included into the model to simulate the stress distribution in the buttress thread and the standard thread, respectively. The FEA model was created in ANSYS Workbench 15.0® software package.[20]

Because of the complexity of the contact stress analysis at the bolted joint regions and the stress concentrations at the thread roots, the stress distribution in these parts is expected to be complex. Therefore, a finer mesh was generated in these parts. For the parts far away from the connections where the stress distribution is simpler, the mesh was coarser in order to

decrease the memory and computational time but still get a relatively accurate result.

A progressively increasing reaction force from the anvils onto the body and the nut was modeled as the load on the cell. The maximum equivalent stress in the thread was found to equal the tensile yield strength of MLS 316L stainless steel when the force of 1.5 kN is applied on the cell with the buttress thread. This is equivalent to an average pressure of 5.2 GPa on the culets of the diamonds. The contact surface between the diamond anvil and the body is chosen as the boundary condition.

B. FEA results

Figure 8 presents the section view of the cell illustrating the stress distribution on the buttress thread at a pressure of 5.2 GPa on the culets. As expected, the simulations show that the maximum stress occurs at the roots of the thread because of the stress concentration. The maximum equivalent stress value in the thread is 675 MPa, which occurs at the top turn of the internal thread in the nut. This value is equal to the material tensile yield stress. Therefore, the maximum average pressure the cell can support with the buttress thread is, in principle, 5.2 GPa. However, according to Sadkov and Solodukhina,[21] the maximum pressure in the sample volume is in practice about three times the averaged pressure on the culet due to the friction between the anvils and the gasket. Therefore, a maximum pressure in excess of 15 GPa can be expected for the critical load of 1.5 kN for 600 μm culets.

In order to compare the performance of the buttress thread and the standard thread, an FEA model with similarly dimensioned standard thread was created. The stress distribution and the comparison between the two models are shown in Figs. 9 and 10, respectively.

Figure 9 shows that the maximum equivalent stress has a value of 742 MPa at the first engaged internal thread. This value is 10% higher than that in the buttress thread model. Fig. 10(a) presents the stress distribution in the internal thread roots. The results are in agreement with Chen's simulations[22] and Yamatoto's method.[23] The stress distribution in the buttress
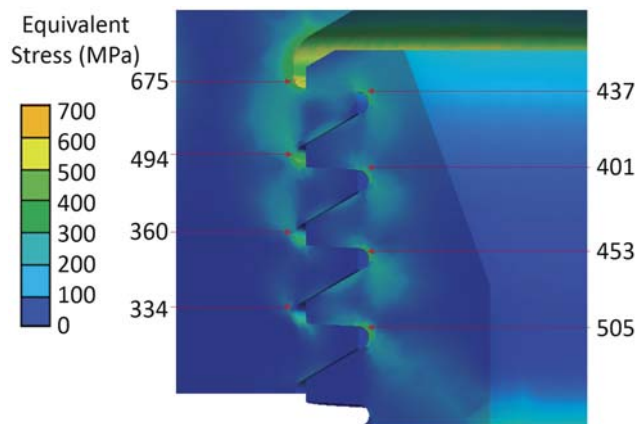

FIG. 8. The equivalent stress distribution in the buttress threads based on the FEA results under the load of 5.2 GPa on the culets. The cross section is chosen where the maximum stress occurs in the first turn of the thread. The maximum stress is 675 MPa, which occurs at the top turn of the internal thread.
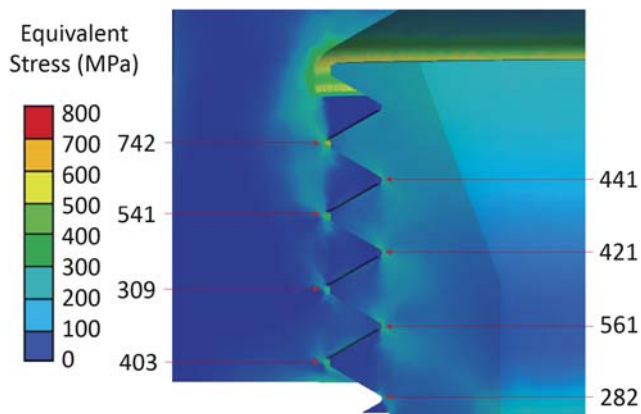
FIG. 9. The equivalent stress distribution in the standard threads based on the FEA results under the same load as in Fig. 8. The cross section is chosen where the maximum stress occurs in the first turn of the thread. The maximum stress is 742 MPa, which occurs at the first engaged internal thread. Due to the shape of the threads, the stress is more localized in the vicinity of the standard thread root; thus the stress distribution in the standard threads is less diffuse than it is in the buttress threads.

thread is more uniform than in the standard thread. Fig. 10(b) shows the stress distribution in the external thread roots. The trend differs from that in the thread connection because the non-uniformity of the hole at the center of the body results in different stiffness in the threaded parts and a reduction of the gradient of the stress distribution in the thread. For the

standard thread, the stress decreases on the 4th thread since the last turn of the thread pair is not fully engaged. As can be seen from the comparison between the buttress thread and the standard thread (Fig. 10(a)), the stress distribution in the buttress thread is more uniform, which gives a lower maximum equivalent stress at the root. This helps to increase the load support capability and the service pressure of the DAC.

IV. EXPERIMENTAL TEST

The cell was constructed from stainless steel 316L by 3D MicroPrint GmbH[18] using the MLS method and then polished. The weight of the 3D-DAC is 2 g, which results in rapid thermal equilibration when exposed to the gas stream of the Cryostream. The cell parts and the assembly are shown in Fig. 11. In all tests, BERYLCO 25 was used as the gasket material, purchased in half-hardened form from NGK Berylco and subsequently heat treated for 2 h at 315 °C for
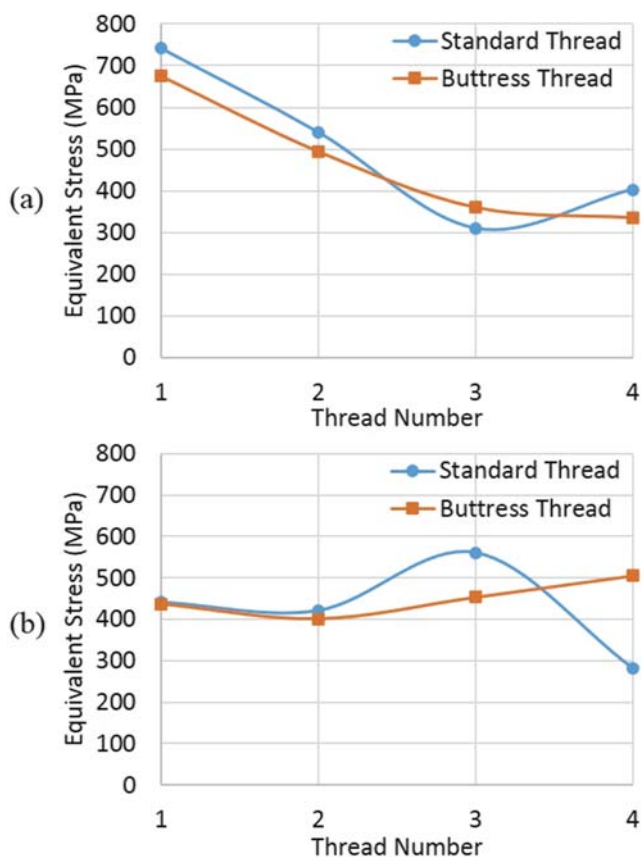

FIG. 10. The comparison of the stress values between the buttress thread and the standard thread. The stress values are sampled at the roots of the thread which have the stress concentration effect. (a) The stress distribution in the internal thread. (b) The stress distribution in the external thread.
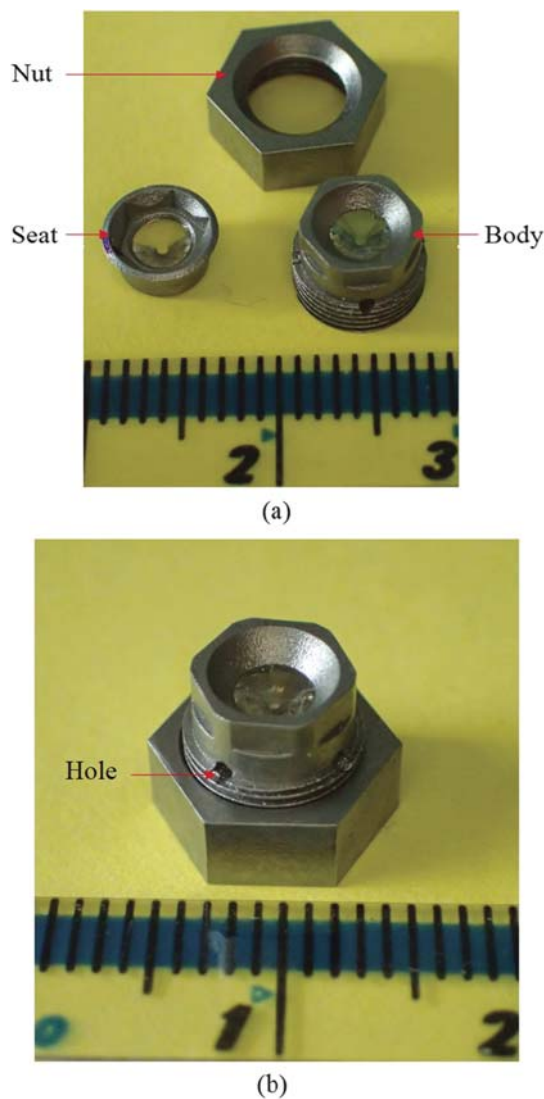

FIG. 11. The cell parts (a) which are constructed by 3D micro laser sintering (b). There are 4 holes with the diameter of 1 mm circumferentially equispaced on the body part for checking the alignment of the diamonds and mounting the DAC on the goniometer head of the diffractometer.
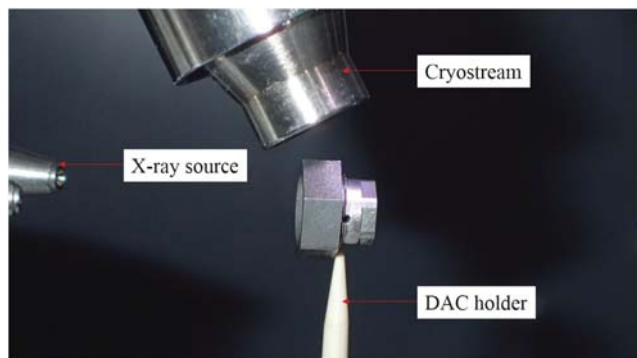
FIG. 12. The DAC in the diffractometer at 120 K. The DAC is mounted on the DAC holder, which is made from polyether ether ketone.

optimal gasket properties. The gaskets were pre-indented to 100 μm with a 150 μm diameter sample hole that was hand-drilled.

A. Pressure test

A pressure test for the DAC was performed prior to any further tests. The diamonds were attached to the body and the seat using a sparing quantity of epoxy glue. Alignment of the anvils was achieved through the precision of manufacturing of the parts. The gasket was placed in the cell and loaded with a single ruby sphere and a 4:1 methanol-ethanol mixture as pressure-transmitting medium (PTM). No lubrication is used on the threads. The load was gradually increased to reach a pressure of 14.5 GPa, as measured by ruby fluorescence.[24] There was no visible damage to or deformation of any parts of the pressure cell.

For the pressure of 14.5 GPa, the applied load as measured by the load cell was 2 kN. The correspondence between the load and the pressure it generated is strictly speaking not reproducible as it is affected by a number of factors such as the gasket material, PTM, the friction between threads, the friction between the press and the clamp, etc. Therefore, the applied load in the experiment might be somewhat different than the load modelled in FEA simulations. However, in addition to allowing to estimate the pressure on the sample, monitoring the allied load with the load cell allows users to monitor and
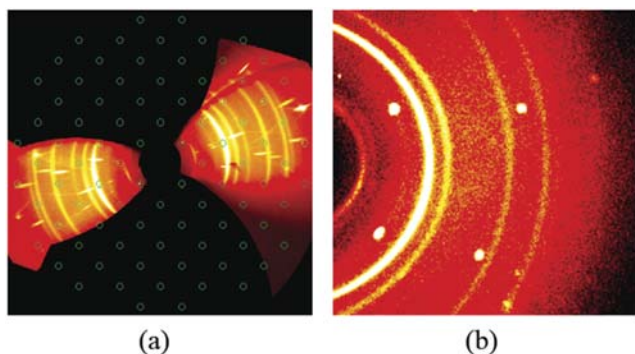

FIG. 13. (a) Axial procession image reconstructed from diffraction data at 1.7 GPa and 120 K. No ice is observed in the diffraction pattern (b) Diffraction image taken at 1.7 GPa and 120 K. Again no ice rings are observed.
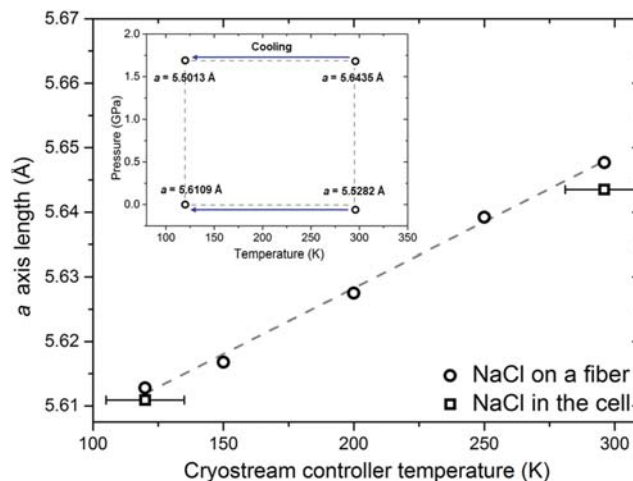

FIG. 14. *a* axis length of NaCl determined on a fiber at a previously calibrated position under an Oxford Cryosystems Cryostream (black circles). The black dashed line is a linear fit to the data. *a* axis length of NaCl determined in the cell at zero pressure (black squares) at 298 K and 120 K. (Inset) Estimated pressures determined from the *a* axis length of NaCl at 298 K and 120 K.

reproduce the locking load in order to change the pressure to a new value.

B. Crystallographic test

Two sets of experiments were carried out in order to determine (i) whether the temperature at the sample is equal to the set-point of the cryostream, (ii) the effect that cooling the cell has on the pressure in the sample cavity, and (iii) whether the cell was capable of producing adequate data for crystallographic structural refinement. In order to address these questions, the cell was loaded with single crystals of sodium chloride (NaCl) and deuterated hexamethylenetetramine (HMT-d_{12}). Initially no pressure-transmitting medium was included to ensure that the sample remained at ambient pressure.

The cell was mounted on a Bruker APEX-II diffractometer and a data collection was performed at room temperature (296 K) using the strategy of Ref. 25. The cryostream was cooled at a rate of 360 K/h to the temperature of 120 K before the cell was re-mounted and allowed to equilibrate for 30 min (Fig. 12). Minimal icing was observed on the cell during the entire course of the experiment (8 h) and no ice rings were detected in the diffraction patterns (Fig. 13).

For the purposes of calibration, the lattice parameter of NaCl was also determined on the same instrument in a series of ambient pressure data collections at 120, 150, 200, 250, and 300 K where the sample was mounted on a fibre. Comparison of the calibration data with the lattice parameters of NaCl determined from the pressure cell measurements indicates that when the cryostat set-point was 120 K, the sample temperature was 120 K ($\pm$15 K) (Fig. 14).

The cell was subsequently disassembled and DAPHNE-7373 PTM, chosen for its known hydrostaticity at low temperature, was introduced as a pressure-transmitting medium.[26] A load was applied on the cell until a pressure of 1.7 GPa was observed via ruby fluorescence. Data collections were then carried out at room temperature and 120 K as described above and the pressure was confirmed to be 1.7 GPa, from

TABLE II. Crystallographic data of HMT-d_{12}.

Temperature (K)	298	120	298	120
Pressure (GPa)	Ambient	Ambient	1.7	1.7
Radiation wavelength (Å)		0.717 03		
Diffractometer		APEX 2		
Crystal system		Cubic (I-43m)		
a (Å)	7.0211(4)	6.6920(6)	6.7499(11)	6.7140(10)
V (Å^3)	346.11(6)	337.44(9)	307.53(15)	302.65(14)
Crystal size (mm)		$0.075 \times 0.075 \times 0.075$		
D_x (Mg m^{-3})	1.345	1.380	1.514	1.538
μ (mm^{-1})	0.090	0.092	0.101	0.102
F(000)	152.0	152.0	152.0	152.0
2θ range min/max	8.21–44.514	8.28–45.752	8.54–46.404	8.586–45.778
Index range	$-6 \leq h \leq 6$,	$-7 \leq h \leq 7$,	$-5 \leq h \leq 5$,	$-7 \leq h \leq 7$,
	$-7 \leq k \leq 7$,	$-6 \leq k \leq 6$,	$-7 \leq k \leq 7$,	$-7 \leq k \leq 7$
	$-6 \leq l \leq 6$	$-6 \leq l \leq 6$	$-7 \leq l \leq 7$	$-5 \leq l \leq 5$
Reflections collected	534	528	479	459
	56	56	52	49
Independent reflections	[R_{int} = 0.0278,	[R_{int} = 0.0172,	[R_{int} = 0.0829,	[R_{int} = 0.0915,
	R_{sigma} = 0.0220]	R_{sigma} = 0.0097]	R_{sigma} = 0.0637]	R_{sigma} = 0.0413]
Data/restraints/parameters	56/0/8	56/0/8	52/0/8	49/0/8
Final R indexes [I $\geq 2\sigma$(I)]	R_1 = 0.0389,	R_1 = 0.0326,	R_1 = 0.0417,	R_1 = 0.0474,
	wR_2 = 0.1103	wR_2 = 0.0731	wR_2 = 0.0823	wR_2 = 0.0763
Final R indices [all data]	R_1 = 0.0486,	R_1 = 0.0357,	R_1 = 0.0948,	R_1 = 0.0707,
	wR_2 = 0.1148	wR_2 = 0.0746	wR_2 = 0.0890	wR_2 = 0.0790
Largest diff. Peak/hole/e Å^{-3}	0.10/−0.18	0.09/−0.15	0.13/−0.18	0.08/−0.12

the NaCl equation of state (EOS).[27] The estimated pressure was further corroborated against the low temperature high-pressure EOS of HMT-d_{12}[28] and found to be consistent within 0.05 GPa.

Structural refinement against the diffraction data for HMT-d_{12} was possible in all cases and provided high-quality structural refinements of atomic positions and thermal parameters of the carbon and nitrogen positions. All four datasets had final R-factors of <5% (Table II and Fig. 15), marginally higher than the datasets collected on a fiber (120 K R_1 = 3.26%; 296 K R_1 = 3.89%).

The 296 K and 120 K refinements at ambient pressure can be directly compared to the equivalent refinements of crystals of HMT-d_{12} mounted on the fiber, in order to estimate the level of error introduced by collecting in this new high-pressure cell. For both atomic positions and U_{eq}, the parameters are consistent within 3 σ.
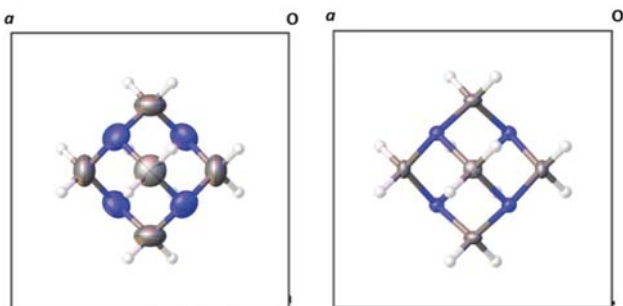

FIG. 15. Structural refined data of HMT-d_{12} at room temperature and pressure (left), and 120 K and 1.7 GPa (right). Atomic displacement ellipsoids are contoured at the 50% probability level.

V. CONCLUSION

A new miniature high-pressure cell was designed and manufactured by the micro laser sintering technique. The additive manufacturing method gives more space for the complex geometry of the cell design. A buttress thread was used in the cell to reduce the stress concentrations and improve the load support capability. The cell was experimentally tested by collecting X-ray diffraction data at low temperature and high pressure. It was established that the sample temperature in the cell is the same as when the sample is measured with conventional mounting at ambient pressure, implying that re-calibration of the cryostat is unnecessary. The metallic construction of the pressure cell body ensures a low temperature gradient within the anvils and the sample cavity. In addition, the sample pressure does not change with temperature on cooling, which we attribute to the interplay between the small size of the components and the thermal expansion coefficients of the materials used in the construction.

FEA simulations indicate that use of a buttress thread enables higher pressures to be attained than with a standard thread, but the use of the micro laser sintering technology is critically important for realizing this advantage in practice. In future work, the profile of the buttress thread will be further optimized using FEA simulations with the aim of forming a higher root circular-arc radius and a greater thickness at the tooth root, enabling the load to be increased over the present design, within an even smaller cell.

The 3D-DAC also shows promise for use in neutron diffraction experiments because of the small wall thicknesses and thus low absorption. The large step in path lengths through

the cell body at the bottom of the nut would complicate the correction for absorption though. Furthermore, with the development of new material powders for the MLS technique, cells can be fabricated with higher strength alloys, such as titanium alloy Ti-6Al-4V.

ACKNOWLEDGMENTS

[1] P. Loubeyre, R. LeToullec, D. Hausermann, M. Manfland, R. J. Hemley, H. K. Mao, and L. W. Finger, Nature **383**, 702 (1996).
[2] L. Merrill and W. A. Basset, Rev. Sci. Instrum. **45**, 290 (1974).
[3] C. Martin, C. C. Agosta, S. W. Tozer, H. A. Radovan, T. Kinoshota, and M. Tokumoto, J. Low Temp. Phys. **138**, 1025 (2005).
[4] D. E. Graf, R. L. Stillwella, K. M. Purcell, and S. Tozer, High Pressure Res. **31**, 533 (2011).
[5] M. Kano, N. Kurita, M. Hedo, Y. Uwatoko, S. W. Tozer, H. S. Suzuki, T. Onimaru, and T. Sakakibara, J. Phys. Soc. Jpn. **76**, 56 (2007).
[6] G. Giriat, W. Wang, J. P. Attfield, A. D. Huxley, and K. V. Kamenev, Rev. Sci. Instrum. **81**, 073905 (2010).
[7] C. J. Ridley and K. V. Kamenev, Z. Kristallogr. **229**, 171 (2014).
[8] J. Binns, K. V. Kamenev, G. J. McIntyre, S. A. Moggach, and S. Parsons, IUCrJ **3**, 168 (2016).
[9] I. Gibson, D. W. Rosen, and B. Stucker, *Additive Manufacturing Technologies* (Springer, New York, 2010).
[10] S. A. Moggach, D. R. Allan, S. Parsons, and J. E. Warren, J. Appl. Crystallogr. **41**, 249 (2008).
[11] W. E. Frazier, J. Mater. Eng. Perform. **23**, 1917 (2014).
[12] G. E. Totten, L. Xie, and K. Funatani, *Handbook of Mechanical Alloy Design* (Marcel Dekker, Inc., New York, 2004), Chap. 7, p. 382.
[13] E. Oberg, F. D. Jones, H. L. Horton, and H. H. Ryffell, *Machinery's Handbook*, 26th ed. (Industrial Press, New York, 2000), Chap. 10, p. 1817.
[14] S. Klotz, G. Hamel, and J. Frelat, High Pressure Res. **24**, 219 (2004).
[15] J. Cosier and A. M. Glazer, J. Appl. Crystallogr. **19**, 105 (1986).
[16] R. Boehler and K. D. Hantsetters, High Pressure Res. **24**, 391 (2004).
[17] R. G. Budynas and J. K. Nisbett, *Shigley's Mechanical Engineering Design*, 9th ed. (McGraw-Hill, Singapore, 2011), Chap. 8, pp. 410–422.
[18] See http://3dmicroprint.com/products/ for 3D MicroPrint GmbH.
[19] X. Wang and K. V. Kamenev, Low Temp. Phys. **40**, 735 (2014).
[20] See http://http://www.ansys.com for ANSYS.
[21] Y. A. Sadkov and L. B. Solodukhina, J. Appl. Mech. Tech. Phys. **33**, 903 (1992).
[22] H. Chen, P. Zeng, G. Fang, and L. Lei, Chin. J. Mech. Eng. **46**, 171 (2010).
[23] A. Yamatoto, *The Theory and Computation of Threads Connection* (Yokendo, Tokyo, 1980).
[24] G. J. Piermarini, S. Block, J. D. Barnett, and R. A. Forman, J. Appl. Phys. **46**, 2774 (1975).
[25] A. Dawson, D. R. Allan, S. Parsons, and M. Ruf, J. Appl. Crystallogr. **37**, 410 (2004).
[26] K. Yokogawa, K. Murata, H. Yoshino, and S. Aoyama, Jpn. J. Appl. Phys. **46**, 3636 (2007).
[27] E. F. Skelton, A. W. Webb, S. B. Qadri, S. A. Wolf, R. C. Lacoe, J. L. Feldman, W. T. Elam, E. R. Carpenter, Jr., and C. Y. Huang, Rev. Sci. Instrum. **55**, 849 (1984).
[28] S. Parsons, personal communication (2016).